Forcing Scale Invariance in Multipolarization
SAR Change Detection

Forcing Scale Invariance in Multipolarization SAR Change Detection

Vincenzo Carotenuto, *Student Member, IEEE*, Antonio De Maio, *Fellow, IEEE*, Carmine Clemente, *Member, IEEE*, John J. Soraghan, *Senior Member, IEEE*, and Giusi Alfano

***Abstract*—This paper considers the problem of coherent (in the sense that both amplitudes and relative phases of the polarimetric returns are used to construct the decision statistic) multipolarization synthetic aperture radar change detection starting from the availability of image pairs exhibiting possible power mismatches/miscalibrations. The principle of invariance is used to characterize the class of scale-invariant decision rules which are insensitive to power mismatches and ensure the constant false alarm rate property. A maximal invariant statistic is derived together with the induced maximal invariant in the parameter space which significantly compresses the data/parameter domain. A generalized likelihood ratio test is synthesized both for the cases of two- and three-polarimetric channels. Interestingly, for the two-channel case, it is based on the comparison of the condition number of a data-dependent matrix with a suitable threshold. Some additional invariant decision rules are also proposed. The performance of the considered scale-invariant structures is compared to those from two noninvariant counterparts using both simulated and real radar data. The results highlight the robustness of the proposed method and the performance tradeoff involved.**

***Index Terms*—Coherent change detection, maximal invariant, multipolarization, scale invariance.**

I. Introduction

A TOPIC of great interest in the remote sensing, signal processing, and synthetic aperture radar (SAR) communities is change detection. This is the ability to identify temporal changes within a given scene starting from a pair of coregistered SAR images representing an area of interest [1], [2]. Incoherent and coherent change detections are the two main approaches that have been proposed in the open literature to process the image pair. The former attempts to detect changes in the mean power level of a given scene, exploiting only the intensity information from the available images (thus neglecting phase information [3]): differencing and rationing are well-known techniques in this context [4]. The latter jointly uses both amplitude and phase from the reference and the test data to detect possible changes in the region of interest. In [3], a thorough comparison between incoherent and coherent change detection strategies, including the maximum likelihood estimate of the SAR coherence parameter, is performed based on high-resolution $(0.3\ \mathrm{m} \times 0.3\ \mathrm{m})$ SAR images. In [4], several techniques for change detection have been presented and compared based on their probability of error and on results obtained using repeat-pass ERS-1 SAR data. In [5]–[7], the multipolarization signal model for the SAR change detection problem is laid down, the detection problem is formulated as a binary hypothesis test, and a decision rule based on the generalized likelihood ratio test (GLRT) is developed. Moreover, the performance analysis [6] of the GLRT is given in the form of receiver operating characteristics (ROC), namely, detection probability (P_d) versus false alarm probability (P_{fa}), quantifying the benefits of the multipolarization information in SAR change detection. A complementary approach to the GLRT is considered in [8] based on the use of perturbation filters and a separated treatment between polarimetry and amplitude.

A detection scheme based on canonical correlation analysis is applied to scalar EMISAR data in [9], [10], whereas in [11], a mutual-information-based framework is developed to address coherent similarities between multichannel SAR images. Starting from the multipolarization data model developed in [5] and [6], in [12] and [13], a new and systematic framework for change detection based on the theory of invariance in hypothesis testing problems is proposed. This setup allows us to focus on decision rules which exhibit some natural symmetries implying important practical properties such as the constant false alarm rate (CFAR) behavior. Furthermore, the use of invariance leads to data reduction because all invariant tests can be expressed in terms of a statistic, called maximal invariant, which organizes the original data into equivalence classes. Also, the parameter space is usually compressed after reduction by invariance, and the dependence on the original set of parameters becomes embodied into a maximal invariant in the parameter space (induced maximal invariant). Starting from the framework proposed in [12], in this paper, we introduce the capability to account for a possible scale mismatch factor.

The new approach is able to produce scale-invariant decision rules, providing advantages in terms of robustness to intensity mismatches and/or miscalibrations and false alarm rejection with respect to [12]. This is an important property as images over the same scene can exhibit different intensity scales due

Manuscript received December 22, 2014; revised April 13, 2015; accepted June 10, 2015. This work was supported in part by the University of Naples "Federico II," in part by the Engineering and Physical Sciences Research Council under Grant EP/K014307/1, in part by the MOD University Defence Research Collaboration in Signal Processing, and in part by the Politecnico di Torino.

V. Carotenuto and A. De Maio are with the Dipartimento di Ingegneria Elettrica e delle Tecnologie dell'Informazione, Università degli Studi di Napoli "Federico II," 80125 Napoli, Italy (e-mail: vincenzo.carotenuto@unina.it; ademaio@unina.it).

C. Clemente and J. J. Soraghan are with the Centre for Excellence in Signal and Image Processing, Department of Electronic and Electrical Engineering, University of Strathclyde, G1 1XW Glasgow, U.K. (e-mail: carmine.clemente@strath.ac.uk; j.soraghan@strath.ac.uk).

G. Alfano is with the Communication Group, Dipartimento di Elettronica e Telecomunicazioni, Politecnico di Torino, 10129 Torino, Italy (e-mail: giuseppa.alfano@polito.it).

Color versions of one or more of the figures in this paper are available online at http://ieeexplore.ieee.org.

Digital Object Identifier 10.1109/TGRS.2015.2449332

to different observation angles and propagation properties. As a matter of fact, there are situations in earth observation where a change detector without scale invariance is likely to fail. A classic example is the sea where different sea states can trigger a detector without scale invariance. Another example is the ground surface that shows very different moisture conditions (due, for instance, to rain). The mentioned effects can often lead to false alarms in a change detection structure that is not designed to be robust with respect to such scale variations. We also compute the GLRT detector and prove that it belongs to the class of scale-invariant decision rules. Interestingly, with reference to two-polarimetric channels, it is tantamount to comparing the condition number of a data-dependent matrix with a suitable threshold.

From a technical (detection theory) point of view, the derivations of the GLRT receiver for the considered problem are, to the best of the authors knowledge, a new result together with the analytic expressions of $P_{\rm fa}$ and P_d (developed in Appendix B) and the determination of the maximal invariant statistic.

At the analysis stage, we assess the performance of the considered invariant decision rules in correspondence of a two- (and three-) channel polarization diversity providing detection probability contours, for a given false alarm level, versus the induced maximal invariant which turns out one- (bi-) dimensional ROC curves and the value of the $P_{\rm fa}$ for different scale values. Finally, to validate the behavior of the considered tests on real SAR images, we use a high-resolution change detection dataset, available from Air Force Research Laboratory (AFRL) [14], [15] and collected from an X-band SAR. The conducted analysis highlights the capability of the proposed detectors to provide scale invariance in real environments and, at the same time, to ensure satisfactory detection performances.

The remainder of this paper is organized as follows. In Section II, we deal with the formulation of the multipolarization SAR change detection problem. In Section III, the maximal invariant for the scale-invariant SAR change detection problem is established. The design of the GLRT and other scale-invariant receivers is presented in Section IV, whereas in Section V, the performance of the introduced invariant tests is shown on both simulated and real multipolarization SAR images. Finally, the conclusion is provided in Section VI.

A. Notation

We adopt the notation of using boldface for vectors and matrices. The transpose and conjugate transpose operators are denoted, respectively, by the symbols $(\cdot)^T$ and $(\cdot)^\dagger$. $\mathrm{tr}(\cdot)$ and $\det(\cdot)$ are, respectively, the trace and the determinant of the square matrix argument. $\boldsymbol{I}$ and $\boldsymbol{0}$ denote, respectively, the identity matrix and the matrix with zero entries (their size is determined from the context). $\mathbf{Diag}(\boldsymbol{a})$ indicates the diagonal matrix whose ith diagonal element is the ith entry of $\boldsymbol{a}$. The curled inequality symbol $\succ$ is used to denote generalized matrix inequality: for any Hermitian matrix $\boldsymbol{A}$, $\boldsymbol{A} \succ \boldsymbol{0}$ means that $\boldsymbol{A}$ is a positive definite matrix. The general linear group of degree N over the field of complex numbers, denoted by $\mathcal{GL}(N)$, is the set of $N \times N$ nonsingular matrices together with the operation of ordinary matrix multiplication. $\mathcal{H}_N^{++}$ and $\mathcal{R}^{++}$ denote, respectively, the set of $N \times N$ Hermitian positive definite matrices and the set of positive real numbers. $\mathbf{1}_N$ is the $N \times 1$ vector with all of the entries equal to one.

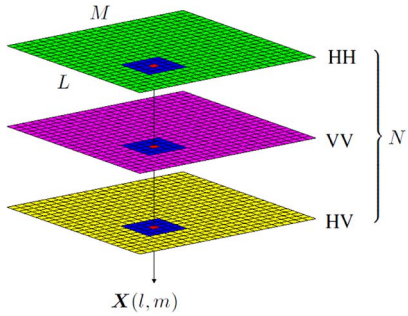

Fig. 1. Construction of the datacube.

II. Problem Formulation

A multipolarization SAR sensor measures for each pixel of the image under test $N \in \{2, 3\}$ complex returns, collected from different polarimetric channels (for instance, HH and VV for $N = 2$; HH, VV, and HV with reference to $N = 3$). The N returns from the same pixel are stacked to form the vector $\boldsymbol{X}(l, m)$, where $l = 1, \ldots, L$ and $m = 1, \ldots, M$ (L and M represent the vertical and horizontal sizes of the image, respectively). Thus, the sensor provides a 3-D data stack $\boldsymbol{X}$ of size $M \times L \times N$ which will be referred to in the following as a datacube (Fig. 1).

For SAR change detection applications, we suppose that two datacubes $\boldsymbol{X}$ (reference data) and $\boldsymbol{Y}$ (test data) of the same geographic area are available; they are collected from two different sensor passes and are quite accurately pixel aligned (coregistered). We focus on the problem of detecting the presence of possible changes in a rectangular neighborhood $\mathcal{A}$, with size $K = W_1 \times W_2 \geq 3$, of a given pixel. To this end, we denote by $\boldsymbol{R}_X$ ($\boldsymbol{R}_Y$) the matrix whose columns are the vectors of the polarimetric returns from the pixels of $\boldsymbol{X}$ ($\boldsymbol{Y}$) which fall in the region $\mathcal{A}$ and $\boldsymbol{S}_X = \boldsymbol{R}_X \boldsymbol{R}_X^\dagger$ ($\boldsymbol{S}_Y = \boldsymbol{R}_Y \boldsymbol{R}_Y^\dagger$).

The matrices $\boldsymbol{R}_X$ and $\boldsymbol{R}_Y$ are modeled as statistically independent random matrices. Moreover, the columns of $\boldsymbol{R}_X$ ($\boldsymbol{R}_Y$) are assumed statistically independent and identically distributed random vectors[1] drawn from a complex circular zero-mean Gaussian distribution with positive definite covariance matrix $\boldsymbol{\Sigma}_X$ ($\boldsymbol{\Sigma}_Y$). From the physical point of view, this is tantamount to assuming a fully developed speckle [16], [17]. Under the aforementioned settings, the change detection problem in the region $\mathcal{A}$ can be formulated in terms of the following binary hypothesis test:

$$\begin{cases} H_0 : \boldsymbol{\Sigma}_X = \gamma \boldsymbol{\Sigma}_Y \\ H_1 : \boldsymbol{\Sigma}_X \neq \gamma \boldsymbol{\Sigma}_Y \end{cases} \tag{1}$$

[1]Spatial independence among the polarimetric returns from different pixels may be somewhat limiting especially in the presence of spatial oversampling and after the processing operations required by geocoding. However, this assumption is usually met in many multilook SAR signal processing techniques in order to obtain analytic tractability. The goodness of the approximation is A POSTERIORI assessed when testing the processors on real data.

where the null hypothesis H_0 of change absence is tested versus the alternative H_1. The parameter $\gamma > 0$ models possible received power variations between two different acquisitions from the same scene, mainly due to misalignment of the flight paths as well as channel propagation effects.

Exploiting the Gaussian assumption, we can write the joint probability density function (pdf) of $\boldsymbol{R}_X$ and $\boldsymbol{R}_Y$ as

$$f_{\boldsymbol{R}_X,\boldsymbol{R}_Y}(\boldsymbol{R}_X,\boldsymbol{R}_Y|H_1,\boldsymbol{\Sigma}_X,\boldsymbol{\Sigma}_Y) = \frac{1}{\pi^{2NK}\det(\boldsymbol{\Sigma}_X\boldsymbol{\Sigma}_Y)^K}\exp\left\{-\mathrm{tr}\left(\boldsymbol{\Sigma}_X^{-1}\boldsymbol{S}_X+\boldsymbol{\Sigma}_Y^{-1}\boldsymbol{S}_Y\right)\right\}. \tag{2}$$

Using the Fisher–Neyman factorization theorem [18], we can claim that a sufficient statistic for (1) is represented by the two sample Grammian matrices $\boldsymbol{S}_X$ and $\boldsymbol{S}_Y$ which are statistically independent and follow a complex Wishart distribution, i.e., [19]

$$f_{\boldsymbol{S}_X}(\boldsymbol{S}_X|H_1,\boldsymbol{\Sigma}_X) = \frac{c_W}{\det(\boldsymbol{\Sigma}_X)^K}\exp\left\{-\mathrm{tr}\left(\boldsymbol{\Sigma}_X^{-1}\boldsymbol{S}_X\right)\right\} \times \det(\boldsymbol{S}_X)^{K-N}, \quad \boldsymbol{S}_X \succ \boldsymbol{0} \tag{3}$$

$$f_{\boldsymbol{S}_Y}(\boldsymbol{S}_Y|H_1,\boldsymbol{\Sigma}_Y) = \frac{c_W}{\det(\boldsymbol{\Sigma}_Y)^K}\exp-\left\{\mathrm{tr}\left(\boldsymbol{\Sigma}_Y^{-1}\boldsymbol{S}_Y\right)\right\} \times \det(\boldsymbol{S}_Y)^{K-N}, \quad \boldsymbol{S}_Y \succ \boldsymbol{0} \tag{4}$$

with c_W being a proper normalization constant. From the sufficient statistic, we can evaluate the optimum Neyman–Pearson detector as the likelihood ratio test (LRT), which, after standard algebra and statistical equivalences, can be recast as

$$\mathrm{tr}\left[\left(\frac{\boldsymbol{\Sigma}_Y^{-1}}{\gamma}-\boldsymbol{\Sigma}_X^{-1}\right)\boldsymbol{S}_X\right] \underset{H_0}{\overset{H_1}{\gtrless}} T_0 \tag{5}$$

where T_0 is the detection threshold. Evidently, test (5) is not uniformly most powerful, and consequently, it is not practically implementable because it requires the knowledge of $\boldsymbol{\Sigma}_X$, γ, and $\boldsymbol{\Sigma}_Y$ which, in realistic applications, are usually unknown.

III. Data Reduction and Invariance Issues

Both hypotheses under test are composite, or otherwise stated, H_0 and H_1 are equivalent to a partition of the parameter space Θ into the two disjoint sets

$$\Theta_0 = \left\{\boldsymbol{\Sigma}_X = \gamma\boldsymbol{\Sigma}_Y, (\boldsymbol{\Sigma}_X,\boldsymbol{\Sigma}_Y,\gamma) \in \mathcal{H}_N^{++}\times\mathcal{H}_N^{++}\times\mathcal{R}^{++}\right\}$$
$$\Theta_1 = \left\{\boldsymbol{\Sigma}_X \neq \gamma\boldsymbol{\Sigma}_Y, (\boldsymbol{\Sigma}_X,\boldsymbol{\Sigma}_Y,\gamma) \in \mathcal{H}_N^{++}\times\mathcal{H}_N^{++}\times\mathcal{R}^{++}\right\}. \tag{6}$$

This formulation indicates that the individual values of the nuisance parameters are irrelevant: one must only discern to which hypothesis they belong to, namely, whether the covariances are proportional or not. This observation highlights that we can cluster the data considering transformations that leave unaltered:

1) the two composite hypotheses, namely, the partition of the parameter space;
2) the families of distributions under the two hypotheses.

This can be achieved through the *principle of invariance* [20] by which we look for transformations that preserve the formal structure of the hypothesis testing problem and, then, for decision rules invariant to them while also acting as a data reduction technique (i.e., leading to an observation space of significantly lower dimensionality than the original one).

It is not difficult to prove that our testing problem is invariant under the group of transformations G acting on the sufficient statistic as[2]

$$G = \left\{g : \boldsymbol{S}_X \to \boldsymbol{B}\boldsymbol{S}_X\boldsymbol{B}^\dagger, \quad \boldsymbol{S}_Y \to a\boldsymbol{B}\boldsymbol{S}_Y\boldsymbol{B}^\dagger, \quad \boldsymbol{B}\in\mathcal{GL}(N), \quad a\in\mathcal{R}^{++}\right\}. \tag{7}$$

In fact, the families of distributions are preserved because, if $\boldsymbol{S}_X$ ($\boldsymbol{S}_Y$) is Wishart distributed, then $\boldsymbol{B}\boldsymbol{S}_X\boldsymbol{B}^\dagger$ ($\boldsymbol{B}\boldsymbol{S}_Y\boldsymbol{B}^\dagger$) is also Wishart with the same scalar parameters and matrix parameter $\boldsymbol{B}^\dagger\boldsymbol{\Sigma}_X\boldsymbol{B}$ ($a\boldsymbol{B}^\dagger\boldsymbol{\Sigma}_Y\boldsymbol{B}$), where $\boldsymbol{B}\in\mathcal{GL}(N)$ and $a > 0$. Moreover, the original partition of the parameter space is left unaltered since, if $\boldsymbol{\Sigma}_X \neq \gamma\boldsymbol{\Sigma}_Y$, then $\boldsymbol{B}\boldsymbol{\Sigma}_X\boldsymbol{B}^\dagger \neq a\gamma\boldsymbol{B}\boldsymbol{\Sigma}_Y\boldsymbol{B}^\dagger$ and, if $\boldsymbol{\Sigma}_X = \gamma\boldsymbol{\Sigma}_Y$, then $\boldsymbol{B}\boldsymbol{\Sigma}_X\boldsymbol{B}^\dagger = a\gamma_1\boldsymbol{B}\boldsymbol{\Sigma}_Y\boldsymbol{B}^\dagger$.

A. Maximal Invariant Design

The invariance property induces a partition of the data space into orbits (or equivalence classes) where, over each orbit, every point is related to every other through a transformation which is a member of the group G. Any statistic that identifies different orbits in a one-to-one way significantly reduces the total amount of data necessary for solving the hypothesis testing problem and constitutes the compressed data set to be used in the design of any invariant detector. This kind of statistics is called maximal invariant since they are constant over each orbit (invariance) while they assume different values on different orbits (maximality).

Formally, a statistic $\mathbf{T}(\boldsymbol{S}_X,\boldsymbol{S}_Y)$ is said to be a maximal invariant with respect to the group of transformations G if and only if:

1) Invariance:
$$\mathbf{T}(\boldsymbol{S}_X,\boldsymbol{S}_Y) = \mathbf{T}\left[g(\boldsymbol{S}_X,\boldsymbol{S}_Y)\right], \ \forall\, g\in G.$$
2) Maximality:
$$\mathbf{T}\left(\boldsymbol{S}_{X_1},\boldsymbol{S}_{Y_1}\right) = \mathbf{T}\left(\boldsymbol{S}_{X_2},\boldsymbol{S}_{Y_2}\right) \text{ implies that } \exists\, g\in G \text{ such that } \left(\boldsymbol{S}_{X_2},\boldsymbol{S}_{Y_2}\right) = g\left(\boldsymbol{S}_{X_1},\boldsymbol{S}_{Y_1}\right).$$

Notice that there are many maximal invariant statistics, but they are equivalent in that they yield statistically equivalent detectors. Moreover, all invariant tests can be expressed as a function of the maximal invariant statistic [21], [22], which, for the problem of interest, is provided by the following.

Proposition 1: A maximal invariant statistic for problem (1) with respect to the group of transformations (7) is the $(N-1)$-dimensional vector

$$\left(\frac{\lambda_2}{\lambda_1},\frac{\lambda_3}{\lambda_1},\ldots,\frac{\lambda_N}{\lambda_1}\right) \tag{8}$$

[2]The proof that (7) is a group is given in Appendix A.

where $\lambda_1 \geq \lambda_2 \geq \cdots \geq \lambda_N$ are the eigenvalues of $\boldsymbol{S}_X \boldsymbol{S}_Y^{-1}$.

Proof: The transformation group G can be obtained as a composition of the subgroups

$$D = \left\{ d : \boldsymbol{S}_X \to \boldsymbol{B}\boldsymbol{S}_X\boldsymbol{B}^\dagger, \quad \boldsymbol{S}_Y \to \boldsymbol{B}\boldsymbol{S}_Y\boldsymbol{B}^\dagger, \quad \boldsymbol{B} \in \mathcal{GL}(N) \right\} \tag{9}$$

$$E = \left\{ e : \boldsymbol{S}_X \to \boldsymbol{S}_X, \quad \boldsymbol{S}_Y \to a\boldsymbol{S}_Y, \quad a \in \mathcal{R}^{++} \right\}. \tag{10}$$

As a consequence, the maximal invariant can be obtained in two steps, each corresponding to a subgroup of G [20]. To this end, a maximal invariant under the group D has been derived in [13] and is given by the eigenvalues $\lambda_1, \ldots, \lambda_N$ of $\boldsymbol{S}_X \boldsymbol{S}_Y^{-1}$. Additionally, $\forall\, e \in E$, namely, $\forall\, a > 0$, if the eigenvalues of $\boldsymbol{S}_{X,1}\boldsymbol{S}_{Y,1}^{-1}$ are equal to those of $\boldsymbol{S}_{X,2}\boldsymbol{S}_{Y,2}^{-1}$, then the eigenvalues of $a^{-1}\boldsymbol{S}_{X,1}\boldsymbol{S}_{Y,1}^{-1}$ coincide with those of $a^{-1}\boldsymbol{S}_{X,2}\boldsymbol{S}_{Y,2}^{-1}$. Now, define the group $E^\star$ of scale change acting on $\boldsymbol{y} = (y_1, \ldots, y_N)^T \in (\mathcal{R}^{++})^N$ as

$$E^\star = \left\{ e^\star : \boldsymbol{y} \to \frac{1}{a}\boldsymbol{y}, \quad a \in \mathcal{R}^{++} \right\} \tag{11}$$

and observe that a maximal invariant with respect to this last group $E^\star$ is

$$\frac{y_2}{y_1}, \ldots, \frac{y_N}{y_1}. \tag{12}$$

Hence, [20, Prop. 2, p. 288] implies that

$$\frac{\lambda_2}{\lambda_1}, \ldots, \frac{\lambda_N}{\lambda_1} \tag{13}$$

is a maximal invariant under G.

As desired, the principle of invariance produces a significant data reduction: the maximal invariant statistic is a real N-dimensional vector, whereas the original sufficient statistic is composed of the two $N \times N$ Grammian matrices $\boldsymbol{S}_X$ and $\boldsymbol{S}_Y$. A useful physical/intuitive meaning of the eigenvalues of $\boldsymbol{S}_X \boldsymbol{S}_Y^{-1}$, which are involved in the computation of the maximal invariant, stems from the observation that they are solutions to suitable optimization problems involving the generalized Rayleigh quotient (i.e., extrema of the backscattering ratio varying the scattering mechanism [23]).

B. Induced Maximal Invariant Design

The data transformation induces a parameter transformation which leaves the two composite hypotheses unaltered. In other words, by the principle of invariance, one partitions also the parameter space into orbits and usually deals with a reduced set of parameters. The relevant parameters are embodied into any *induced maximal invariant*, namely, any function of the parameters that is constant over each orbit of the parameter space (invariance) but assumes different values over different orbits (maximality).

For the case at hand, an induced maximal invariant is composed of $(\delta_2/\delta_1, \ldots, \delta_N/\delta_1)$, where $\boldsymbol{\delta} = [\delta_1, \ldots, \delta_N]^T$, $\delta_1 \geq \delta_2 \geq \cdots \geq \delta_N$, are the eigenvalues of the matrix

$$\boldsymbol{\Sigma}_X \boldsymbol{\Sigma}_Y^{-1}. \tag{14}$$

The proof of this claim can be done following the same steps as in the proof of Proposition 1, and it has been omitted for the sake of compactness. The physical interpretation of the induced maximal invariant components follows from the observation that they are related to the spread among the backscattering ratios associated with two different scattering mechanisms.

The previous observation highlights that the principle of invariance also yields a significant reduction of the number of the parameters: in fact, the induced maximal invariant is an $(N-1)$-dimensional vector, while the original parameter space was composed of the two covariance matrices $\boldsymbol{\Sigma}_X$, $\boldsymbol{\Sigma}_Y$, and γ.

We explicitly observe that, in the reduced parameter space, the partition corresponding to the two composite hypotheses of the test (1) is $\Xi_0 = \{\mathbf{1}_{N-1}\}$, relative to $\boldsymbol{\Sigma}_X = \gamma\boldsymbol{\Sigma}_Y$, and $\Xi_1 = \overline{\{\mathbf{1}_{N-1}\}}$, relative to $\boldsymbol{\Sigma}_X \neq \gamma\boldsymbol{\Sigma}_Y$, where $\overline{\{\mathbf{1}_{N-1}\}}$ is the set of the $(N-1)$-dimensional column vectors with positive elements and at least one entry different from 1. The structure of Ξ_0, which now corresponds to a simple H_0 hypothesis, clearly shows that all invariant receivers that process a maximal invariant statistic through a transformation independent of $(\omega_1, \ldots, \omega_{N-1}) = (\delta_2/\delta_1, \ldots, \delta_N/\delta_1)$ achieve the CFAR property with respect to both γ and $\boldsymbol{\Sigma}_X$.

IV. GLRT Derivation

This section is devoted to the derivations of the GLRT detector for the considered problem. Precisely, it is considered the decision rule shown in (15), at the bottom of the page, which, after the optimizations over $\boldsymbol{\Sigma}_X$ and $\boldsymbol{\Sigma}_Y$ at the numerator and over $\boldsymbol{\Sigma}_Y$ at the denominator, can be recast (after some algebra and statistical equivalences) as

$$\frac{\min\limits_{\gamma>0}\left[\gamma^N \det^2\left(\frac{\boldsymbol{S}_X}{\gamma} + \boldsymbol{S}_Y\right)\right]}{\det(\boldsymbol{S}_X)\det(\boldsymbol{S}_Y)} \underset{H_0}{\overset{H_1}{\gtrless}} T_1 \tag{16}$$

or equivalently as

$$\frac{\min\limits_{\gamma>0}\left[\gamma^N \det^2\left(\frac{\boldsymbol{S}_Y^{-\frac{1}{2}}\boldsymbol{S}_X\boldsymbol{S}_Y^{-\frac{1}{2}}}{\gamma} + \boldsymbol{I}\right)\right]}{\det\left(\boldsymbol{S}_Y^{-\frac{1}{2}}\boldsymbol{S}_X\boldsymbol{S}_Y^{-\frac{1}{2}}\right)} \underset{H_0}{\overset{H_1}{\gtrless}} T_1 \tag{17}$$

where T_1 is a suitable modification of the original threshold T in (15). In order to proceed further, we have to distinguish

$$\frac{\max\limits_{\boldsymbol{\Sigma}_X}\max\limits_{\boldsymbol{\Sigma}_Y} \frac{1}{(\pi)^{2NK}\det^K(\boldsymbol{\Sigma}_X)\det^K(\boldsymbol{\Sigma}_Y)} \exp\left[-\mathrm{tr}\left(\boldsymbol{\Sigma}_X^{-1}\boldsymbol{S}_X + \boldsymbol{\Sigma}_Y^{-1}\boldsymbol{S}_Y\right)\right]}{\max\limits_{\gamma>0}\max\limits_{\boldsymbol{\Sigma}_Y} \frac{1}{(\pi)^{2NK}\gamma^{NK}\det^{2K}(\boldsymbol{\Sigma}_Y)} \exp\left[-\mathrm{tr}\left(\boldsymbol{\Sigma}_Y^{-1}\left(\frac{\boldsymbol{S}_X}{\gamma} + \boldsymbol{S}_Y\right)\right)\right]} \underset{H_0}{\overset{H_1}{\gtrless}} T \tag{15}$$

between the cases of two- $(N = 2)$ and three- $(N = 3)$ polarimetric channels.

A. Case $N = 2$

Forcing $N = 2$ in (16) yields

$$\frac{\min\limits_{\gamma>0}\left[\gamma^2\left(\frac{\lambda_1}{\gamma}+1\right)^2\left(\frac{\lambda_2}{\gamma}+1\right)^2\right]}{\lambda_1\lambda_2}\underset{H_0}{\overset{H_1}{\gtrless}}T_1. \tag{18}$$

It is now necessary to compute

$$\min_{\gamma>0}\left[\frac{1}{\gamma}\left(\lambda_1\lambda_2+\gamma^2+(\lambda_1+\lambda_2)\gamma\right)\right]^2. \tag{19}$$

Standard arguments on optimization of univariate functions provide the optimal point $\gamma_{\mathrm{opt},2}=\sqrt{\lambda_1\lambda_2}$. As a consequence, the GLRT becomes

$$\left(\sqrt{\frac{\lambda_1}{\lambda_2}}+1\right)^2\left(\sqrt{\frac{\lambda_2}{\lambda_1}}+1\right)^2\underset{H_0}{\overset{H_1}{\gtrless}}T_1. \tag{20}$$

Observing that the left-hand side of (20) is a monotone increasing function of $\sqrt{\lambda_1/\lambda_2}$ for $\sqrt{\lambda_1/\lambda_2}\in[1,+\infty[$, the GLRT (20) turns out equivalent to

$$\frac{\lambda_1}{\lambda_2}\underset{H_0}{\overset{H_1}{\gtrless}}T_2 \tag{21}$$

with T_2 being the modified threshold. Two important comments are now in order. First, test (21) is equivalent to comparing the condition number of the matrix $\boldsymbol{S}_Y^{-(1/2)}\boldsymbol{S}_X\boldsymbol{S}_Y^{-(1/2)}$ with a detection threshold to establish the presence of changes in the considered scene. Second, the GLRT statistic is a maximal invariant.

B. Case $N = 3$

Forcing $N = 3$ in (16) yields

$$\frac{\min\limits_{\gamma>0}\left[\gamma^3\left(\frac{\lambda_1}{\gamma}+1\right)^2\left(\frac{\lambda_2}{\gamma}+1\right)^2\left(\frac{\lambda_3}{\gamma}+1\right)^2\right]}{\lambda_1\lambda_2\lambda_3}\underset{H_0}{\overset{H_1}{\gtrless}}T. \tag{22}$$

It is thus necessary to solve the optimization problem

$$\min_{\gamma>0}\left[\gamma^{\frac{3}{2}}\left(\frac{\lambda_1}{\gamma}+1\right)\left(\frac{\lambda_2}{\gamma}+1\right)\left(\frac{\lambda_3}{\gamma}+1\right)\right]^2=\min_{\gamma>0}f_3(\gamma). \tag{23}$$

Since

$$\lim_{\gamma\to+\infty}f_3(\gamma)=+\infty,\qquad\lim_{\gamma\to0}f_3(\gamma)=+\infty \tag{24}$$

and $f_3(\gamma)$ is continuous in $]0,+\infty[$, the minimum is achieved in correspondence of $\gamma_{\mathrm{opt}}\in]0,+\infty[$. Moreover, finding the optimum value of $f_3(\gamma)$ is equivalent to minimizing its logarithm, i.e.,

$$\log f_3(\gamma)=\frac{3}{2}\log\gamma+\sum_{i=1}^{3}\log\left(\frac{\lambda_i}{\gamma}+1\right). \tag{25}$$

Computing the derivative of $\log f_3(\gamma)$, $\gamma\in]0,+\infty[$, and equating it to zero yields

$$\frac{3}{2}-\sum_{i=1}^{3}\frac{\lambda_i}{\lambda_i+\gamma}=0 \tag{26}$$

which is tantamount to solving

$$\gamma^3+\frac{1}{3}(\lambda_1+\lambda_2+\lambda_3)\gamma^2-\frac{1}{3}(\lambda_1\lambda_2+\lambda_1\lambda_3+\lambda_2\lambda_3)\gamma-\lambda_1\lambda_2\lambda_3=0. \tag{27}$$

This is a third-order equation with real coefficients. Descartes' rule of signs implies that it shares one positive real root which necessarily coincides with the optimal point of (23). Additionally, Tartaglia's formula can be exploited to obtain the analytic expression of the optimizer $\gamma_{\mathrm{opt},3}$. Precisely, denoting by $a=1/3(\lambda_1+\lambda_2+\lambda_3)$, $b=-(1/3)(\lambda_1\lambda_2+\lambda_1\lambda_3+\lambda_2\lambda_3)$, $c=-\lambda_1\lambda_2\lambda_3$, $p=-a^2/3+b$, and $q=2a^3/27-ab/3+c$, the optimal point is the real positive number chosen among the three roots of (27) given by

$$-\frac{a}{3}+\sqrt[3]{-\frac{q}{2}+\sqrt{\frac{q^2}{4}+\frac{p^3}{27}}}+\sqrt[3]{-\frac{q}{2}-\sqrt{\frac{q^2}{4}+\frac{p^3}{27}}}$$

where $\sqrt[3]{(\cdot)}$ and $\sqrt{(\cdot)}$ are complex roots.[3]

Summarizing, the GLRT can be computed as

$$\frac{\left[\gamma_{\mathrm{opt},3}^3\left(\frac{\lambda_1}{\gamma_{\mathrm{opt},3}}+1\right)^2\left(\frac{\lambda_2}{\gamma_{\mathrm{opt},3}}+1\right)^2\left(\frac{\lambda_3}{\gamma_{\mathrm{opt},3}}+1\right)^2\right]}{\lambda_1\lambda_2\lambda_3}\underset{H_0}{\overset{H_1}{\gtrless}}T. \tag{28}$$

An equivalent expression in terms of the maximal invariant can be also obtained. From (27), it can be shown that

$$\gamma_{\mathrm{opt},3}=\lambda_1 h\left(\frac{\lambda_2}{\lambda_1},\frac{\lambda_3}{\lambda_1}\right) \tag{29}$$

with $h(\cdot,\cdot)$ being a suitable bidimensional real function of two real variables. Hence, the GLRT statistic as a function of the maximal invariant can be obtained by substituting (29) in (28).

C. Additional Suboptimum Invariant Detectors

This section presents additional suboptimum invariant detectors with reference to the fully polarimetric processing (i.e., $N = 3$). They exploit suitable combinations of the maximal invariant components and, based on extensive numerical analysis, are seen to achieve satisfactory detection performances. Two chosen combination rules are the standard arithmetic mean and geometric mean which, respectively, lead to the tests

$$\frac{\lambda_1}{\lambda_2}+\frac{\lambda_1}{\lambda_3}\underset{H_0}{\overset{H_1}{\gtrless}}T_a, \tag{30}$$

$$\frac{\lambda_1}{\lambda_2}\frac{\lambda_1}{\lambda_3}\underset{H_0}{\overset{H_1}{\gtrless}}T_b \tag{31}$$

[3]Given a complex number $y=\rho\exp(j\theta)$, the nth roots are $u_k=\rho^{1/n}[\cos(\theta/n+(2\pi k/n))+j\sin(\theta/n+(2\pi k/n))]$, $k=0,1,\ldots,n-1$.

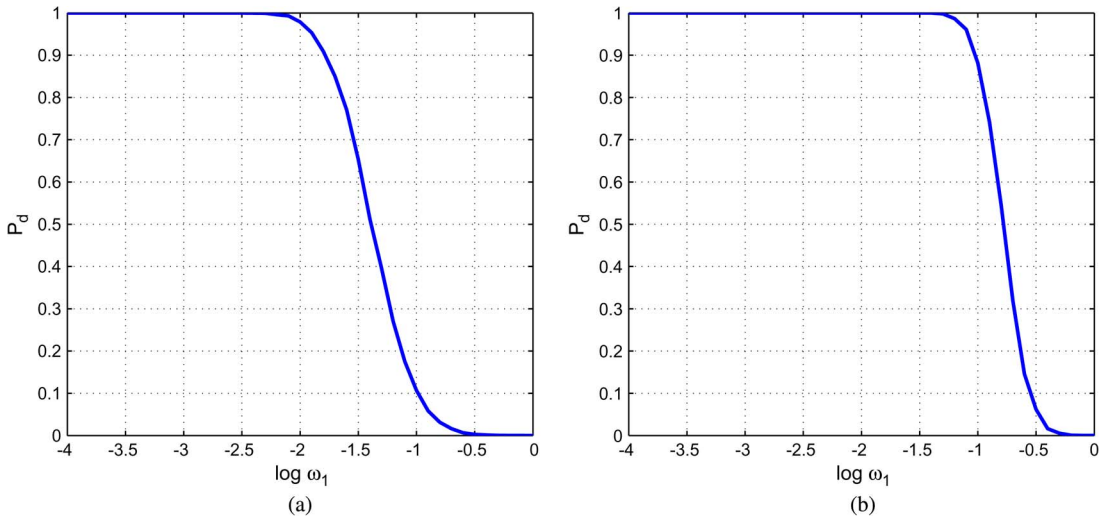

Fig. 2. (a) P_d versus $\log\omega_1$, $N=2$ and $W=3$. (b) P_d versus $\log\omega_1$, $N=2$ and $W=5$.

where T_a and T_b are the detection thresholds set to ensure a specified level of $P_{\rm fa}$.

Moreover, based on the observations that unbalances among the eigenvalues of $\boldsymbol{\Sigma}_Y^{-(1/2)}\boldsymbol{\Sigma}_X\boldsymbol{\Sigma}_Y^{-(1/2)}$ are representative of changes between the reference and test images and an index to quantify eigenvalues' unbalances is the deviation of the arithmetic mean from the geometric mean,[4] the following decision rule is also considered:

$$\frac{\mathrm{tr}\left(\boldsymbol{S}_Y^{-\frac{1}{2}}\boldsymbol{S}_X\boldsymbol{S}_Y^{-\frac{1}{2}}\right)}{\det^{\frac{1}{3}}\left(\boldsymbol{S}_Y^{-\frac{1}{2}}\boldsymbol{S}_X\boldsymbol{S}_Y^{-\frac{1}{2}}\right)}=\left(\frac{\lambda_2}{\lambda_1}\frac{\lambda_3}{\lambda_1}\right)^{-\frac{1}{3}}\left(1+\frac{\lambda_2}{\lambda_1}+\frac{\lambda_3}{\lambda_1}\right)\underset{H_0}{\overset{H_1}{\gtrless}}T_c \tag{32}$$

where T_c is the detection threshold.

In the next section, the performance of the previously introduced invariant (and hence CFAR) decision rules is compared with the GLRT (28) both on simulated and real data.

V. Performance Analysis

This section presents the performance analysis of the proposed scale-invariant detectors for both simulated and real data. In particular, $P_{\rm fa}$ and P_d are obtained through Monte Carlo simulations.[5] Then, real data are used to demonstrate the capability of the new algorithms to operate in real challenging environments.

A. Performance Analysis on Simulated Data

This section presents the performance analysis via computer-simulated data of the detectors introduced in Section IV. Three different studies are performed to assess the properties of the proposed receivers.

[4]If $\boldsymbol{A}$ is a positive definite $N\times N$ matrix, the following inequality holds true $[\det(\boldsymbol{A})]^{1/N}\leq(1/N)\mathrm{tr}(\boldsymbol{A})$. Equality holds if and only if $\boldsymbol{A}=\boldsymbol{I}$ [24, p. 477] .

[5]The only exception where an analytic performance derivation can be carried on is the GLRT for $N=2$ (21). See Appendix B for details.

The first is conducted in terms of P_d for a given $P_{\rm fa}$ level, assuming zero-mean complex circular multivariate Gaussian observations with equal (but not proportional) covariance matrices under H_0 (H_1). By doing so, all of the information characterizing the set of polarimetric SAR images is contained in the covariance matrix. This is equivalent to assigning the following: 1) diagonal elements: power information and 2) off-diagonal elements: correlation information. Different numbers of polarizations and sizes of the square inspection window (i.e., $W_1=W_2=W$) are considered. Monte Carlo simulation is used to set the detection thresholds, assuming $100/P_{\rm fa}$ independent runs and considering a $P_{\rm fa}=10^{-4}$. The value of P_d is estimated using 5000 independent trials.

The first study refers to $N=2$; in this case, the maximal invariant, which completely governs the performance of any invariant detector, is 1-D. This means that the P_d plots versus the induced maximal invariant $\omega_1=\delta_2/\delta_1\leq 1$ completely characterize the performance of detector (21). In other words, the reported performances hold for any pair of covariances $(\boldsymbol{\Sigma}_X;\boldsymbol{\Sigma}_Y)$ sharing the same induced maximal invariant. This is a consequence of the fact that the performance of invariant detectors depends on the pair $(\boldsymbol{\Sigma}_X;\boldsymbol{\Sigma}_Y)$ only through the induced maximal invariant.

In Fig. 2(a) and (b), the values of P_d for $W=3$ and $W=5$ are drawn versus ω_1. For $W=3$, the receiver (21) provides a $P_d\geq 0.9$ for $\omega_1\notin[10^{-1.8},1]$. The case $W=5$ makes use of a greater number of homogeneous data vectors in the Grammians $\boldsymbol{S}_X$ and $\boldsymbol{S}_Y$ whose scaled versions ($1/K$ scale factor) are unbiased and consistent estimates of the covariance matrices $\boldsymbol{\Sigma}_X$ and $\boldsymbol{\Sigma}_Y$. For this situation, a $P_d\geq 0.9$ is achieved for $\omega_1\notin[10^{-1.02},1]$.

A similar analysis is performed for $N=3$ and $W=3$, shown in Fig. 3. In this case, the contours showing P_d are functionally dependent on two variables (namely, the two components of the induced maximal invariant $\boldsymbol{\omega}$): $\omega_1=\delta_2/\delta_1\leq 1$, and $\omega_2=\delta_3/\delta_1\leq 1$. In Fig. 3(a), the contour plot for detector (28) is shown; for this scenario, $P_d\geq 0.9$ is guaranteed if $\omega_i\notin[10^{-2.11},1]$, $i=1,2$. The results for detector (30) are shown

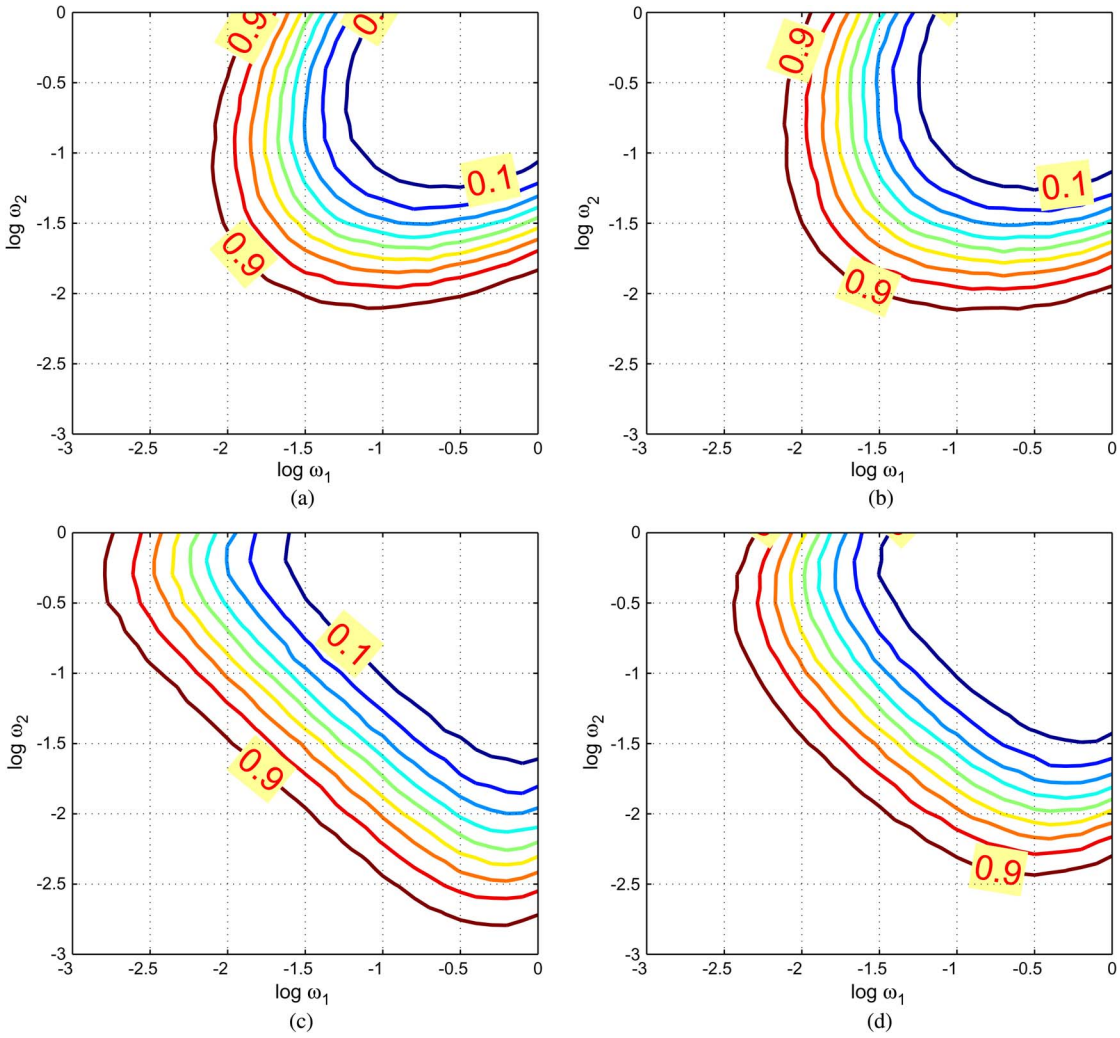

Fig. 3. P_d contours versus $\log \omega_1$ and $\log \omega_2$ for $N = 3$ and $W = 3$. (a) Detector (28). (b) Detector (30). (c) Detector (31). (d) Detector (32).

in Fig. 3(b); in this case, an acceptable P_d is achieved for $\omega_i \notin [10^{-2.14}, 1]$, $i = 1, 2$. For the decision rules (31) and (32), whose results are displayed in Fig. 3(c) and (d), a $P_d \geq 0.9$ is guaranteed for $\omega_i \notin [10^{-2.83}, 1]$ and $\omega_i \notin [10^{-2.46}, 1]$, $i = 1, 2$, respectively.

The contour plots for $N = 3$ and $W = 5$ are shown in Fig. 4; the main difference with the case $W = 3$ is the increase in the detection performance, as observed for the $N = 2$ analysis. In particular, the region in the (ω_1, ω_2) space where P_d is greater than 0.9 grows, e.g., for the decision rule (28), the region is now described by the values $\omega_i \notin [10^{-1.1}, 1]$, $i = 1, 2$.

The second analysis is conducted in terms of ROC curves (namely, P_d versus P_{fa}) for a fixed value of the induced maximal invariant $\boldsymbol{\omega} = [0.04, 0.03]^T$, corresponding to the pair of covariance matrices

$$\boldsymbol{C}_1 = \begin{pmatrix} 16 & 0 & 0.7 \\ 0 & 0.2 & 0 \\ 0.7 & 0 & 1 \end{pmatrix} \quad \boldsymbol{C}_2 = 2 \begin{pmatrix} 4 & 0 & 0.1 \\ 0 & 1.5 & 0 \\ 0.1 & 0 & 6 \end{pmatrix}.$$

Of course, any other covariance pair with the same value of $\boldsymbol{\omega}$ leads to the same ROCs, while a different value of $\boldsymbol{\omega}$ leads to different ROCs. For comparison purposes, the ROCs of the detector (7) in [12] and of that in [6] are also reported. Specifically, the decision rule proposed in [6] is an adaptive implementation of the LRT, whose expression in terms of the eigenvalues $\lambda_1, \ldots, \lambda_N$ is [6, eq. (B-5)]

$$\sum_{i=1}^{N} \left(\frac{1}{\lambda_i} - \ln \frac{1}{\lambda_i} \right) \underset{H_0}{\overset{H_1}{\gtrless}} T_H \tag{33}$$

whereas the GLRT (also [5, eq. (15)], [7, eq. (6)], [11, eq. (20)], and [12, eq. (7)]) is

$$\prod_{i=1}^{N} \frac{(1+\lambda_i)^2}{\lambda_i} \underset{H_0}{\overset{H_1}{\gtrless}} T_g. \tag{34}$$

In order to set the detection thresholds, Monte Carlo simulations were used assuming $100/P_{\text{fa}}$ independent runs. Additionally, 100 000 independent trials were exploited to estimate the P_d.

Fig. 5 shows the ROCs of the considered receivers for both two- and three-polarimetric channels and $W = 3$. In particular, Fig. 5(a) shows the two-polarization case, while Fig. 5(b) refers to the $N = 3$ case. In all of the analyzed situations, the ROC

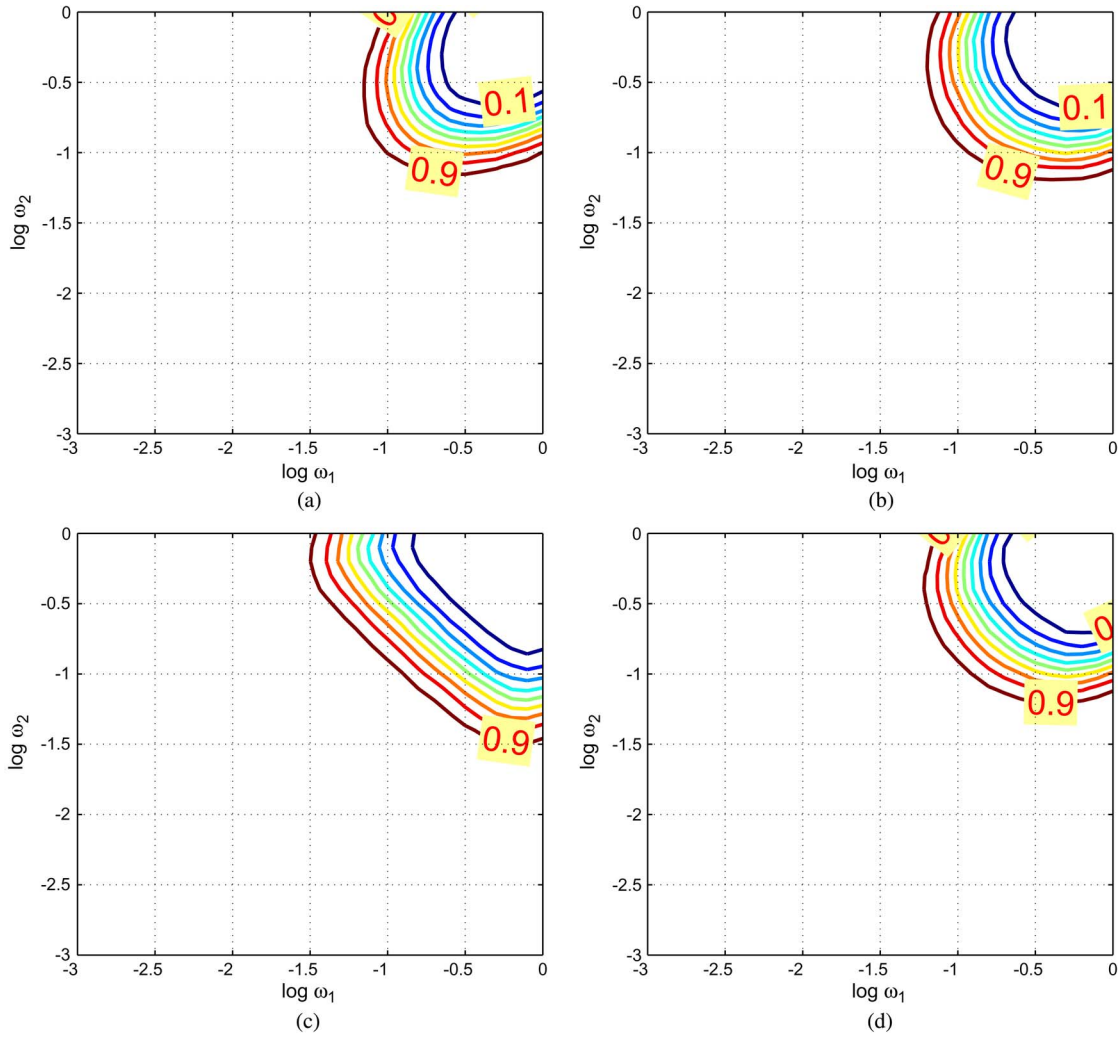

Fig. 4. P_d contours versus $\log \omega_1$ and $\log \omega_2$ for $N = 3$ and $W = 5$. (a) Detector (28). (b) Detector (30). (c) Detector (31). (d) Detector (32).

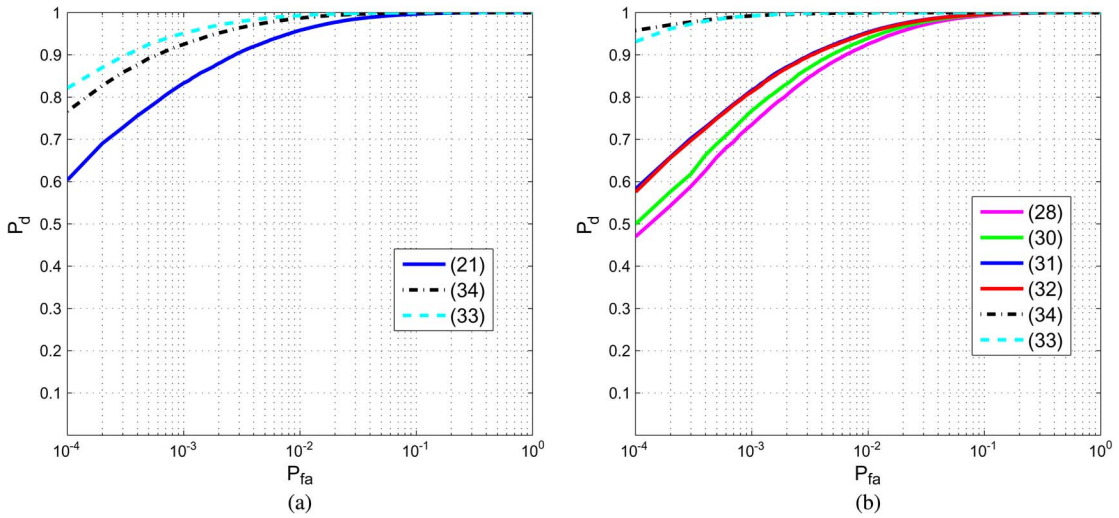

Fig. 5. P_d versus $P_{\rm fa}$. (a) $N = 2, W = 3$. (b) $N = 3, W = 3$.

highlights that the scale-invariant detectors are outperformed in terms of P_d by the two receivers proposed in [12] and in [6] if $W = 3$. However, as soon as $W = 5$, all of the receivers provide the unit P_d value for $P_{\rm fa} \in [10^{-4}, 1]$. This behavior is actually expected as, at the design stage, we are requiring "more invariance" than the detectors (33) and (34). In fact, the new

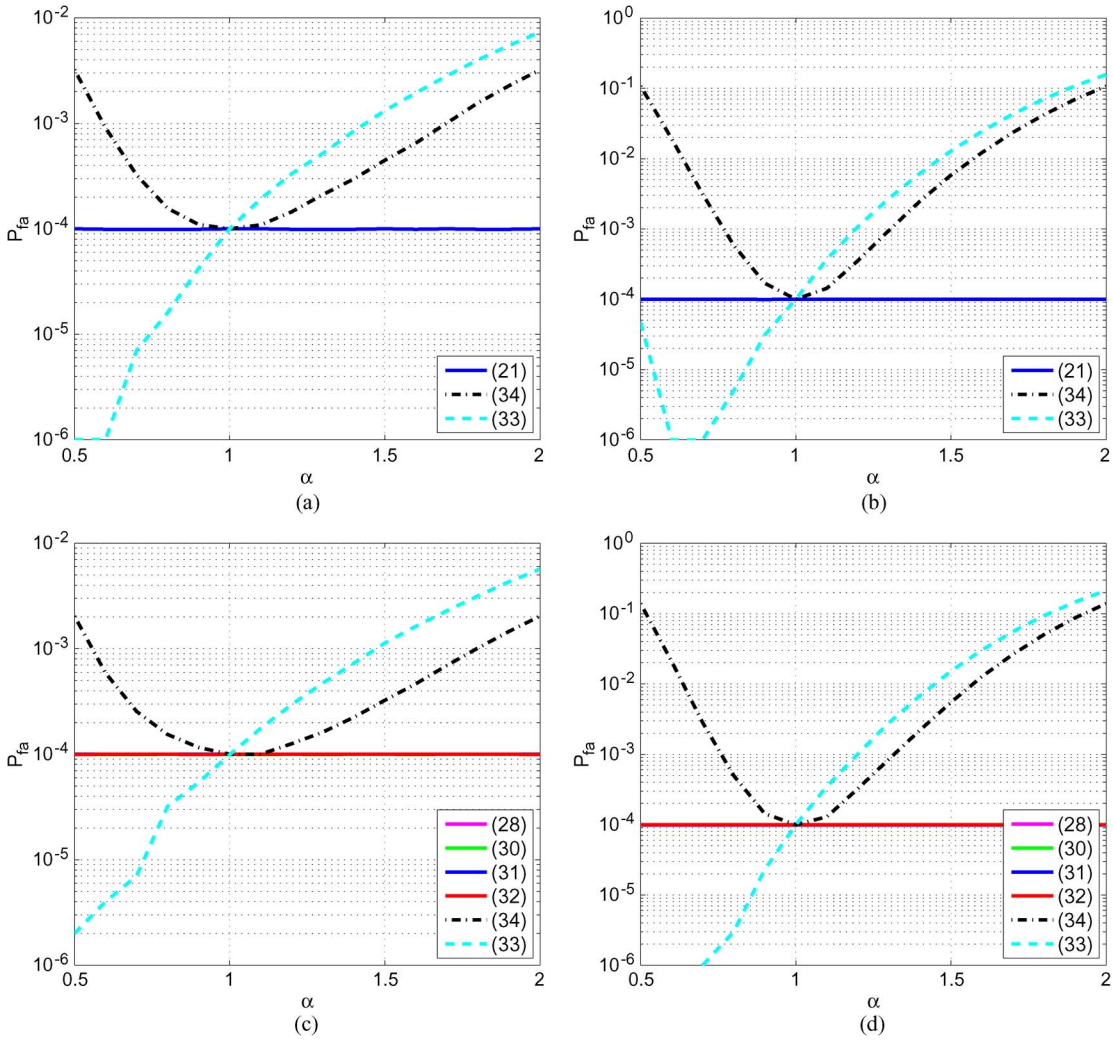

Fig. 6. $P_{\rm fa}$ versus α. (a) $N = 2, W = 3$. (b) $N = 2, W = 5$. (c) $N = 3, W = 3$. (d) $N = 3, W = 5$.

decision rules exhibit an additional scale invariance attempting to robustify the CFAR property with respect to possible scale mismatches between the reference and test images. In other words, as it will also be clearer at the end of this section, with the new approach, we are trading off detection performance with an improved CFAR behavior.

The final analysis assesses the benefits of the proposed approach in terms of CFAR property. The study is conducted considering a nominal $P_{\rm fa} = 10^{-4}$ in the presence of observations with equal covariance matrices (i.e., assuming $C_1 = C_2$). To estimate the actual $P_{\rm fa}$, the covariance matrix C_1 is the same used for the ROC analysis, while C_2 is selected as $C_2 = \alpha C_1$, with $\alpha \in [0.5, 2]$. The nominal threshold for a $P_{\rm fa} = 10^{-4}$ is then used to estimate the actual $P_{\rm fa}$ for each detector.

In Fig. 6, $P_{\rm fa}$ versus α for $N = 2$ and $N = 3$ with inspection window sizes $W = 3$ and $W = 5$ is shown. Also for this analysis, the curves for the detectors (33) and (34) are represented. In all of the considered situations, the invariant detectors show a stable actual probability of false alarm at 10^{-4} (all of their $P_{\rm fa}$ curves overlap with the horizontal line at 10^{-4}). The detectors (33) and (34) exhibit poor capability in handling scale variations between the reference and test images, providing an actual $P_{\rm fa}$ different from the nominal value when a scale variation is present ($\alpha \neq 1$). For example, in the case $N = 3$ and $W = 5$, the detector (34) exhibits an actual $P_{\rm fa}$ of 0.139 for $\alpha = 2$, while the proposed invariant rules are still able to perform with an actual $P_{\rm fa}$ of 10^{-4} as predicted by the developed theory.

B. Performance Analysis on Real Data

The analysis was performed using real X-band data; the dataset used is the coherent change detection challenge dataset acquired by the AFRL [14], [15]. The airborne SAR used to acquire the dataset employed a coherent receiver with 640-MHz bandwidth and dual-polarized mode. The depression angle was 45° for all of the images to scene center. The data are in the form of focused complex images with a range and cross-range resolution of 0.3 m. The overall dataset provides ten complex images for each of the three available polarizations (HH, VV, and HV), acquired the same day. The original image size is 4501×4501 pixels and has been coherently aligned to a single reference (per polarization) with the help of digital elevation map information [14].

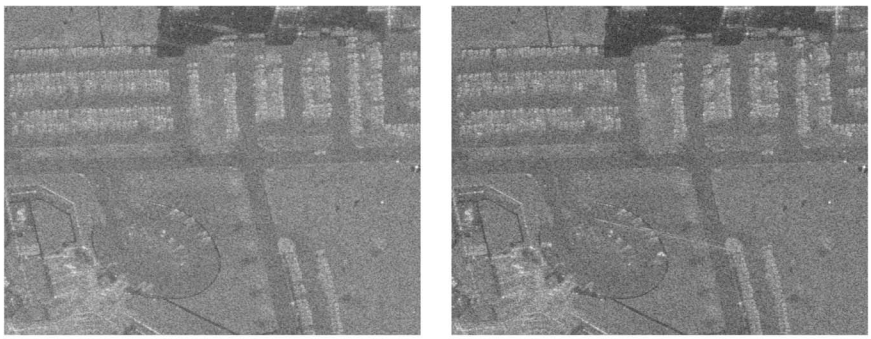

(a) (b)

Fig. 7. Reference and test images gathered in HH mode. (a) Reference image. (b) Test image.

For our analysis, we focus on two acquisitions from the entire dataset. Unfortunately, the ground truths of the data are not available (e.g., the actual changes between two different acquisitions), so the selection of two passes providing the opportunity to generate a sufficiently accurate ground truth is required. Hence, two passes satisfying this requirement have been identified: the acquisition named "FP0124" is used as a reference pass, while the acquisition "FP0121" is used as a test pass. From the two acquisitions, the area with the highest activity (changes) between the images has been selected, and this region is represented by a subimage of 1000×1000 pixels (i.e., $L = M = 1000$) and is composed of several parking lots which are occupied by numerous parked (i.e., stationary) vehicles. Fig. 7 shows the reference and test subimages for the HH mode.

For this particular scenario, the changes between the reference and test images (denoted by $\boldsymbol{X}$ and $\boldsymbol{Y}$, respectively), which occurred during the time interval between the two acquisitions, can be distinguished in two cases.

1) A vehicle is present in $\boldsymbol{X}$ but is not present in $\boldsymbol{Y}$, i.e., the vehicle has departed from its parking space (the pixels relative to this kind of event will be referred to in the following as departures).
2) A vehicle is not present in $\boldsymbol{X}$ but is present in $\boldsymbol{Y}$, i.e., the vehicle has arrived in an empty parking space (the pixels relative to this kind of event will be referred to in the following as arrivals).

Using the cases defined previously, a total of 34 changes between $\boldsymbol{X}$ and $\boldsymbol{Y}$ can be visually identified (by flickering the two images). In the analysis, the straight line crossing the test image has not been considered, as its nature does not represent an arrival. However, as it is visible in the test image (but not visible in the reference image), we expect it to be detected as a change. The obtained empirical ground truth is shown in Fig. 8, where the black regions represent the departures and the white ones indicate the arrivals. In particular, denoting by $\mathcal{K}$ the set of pixels that correspond to changes, the empirical ground truth can be represented as a matrix $\boldsymbol{G}$ whose entries are given by

$$\boldsymbol{G}(l,m) = \begin{cases} 1 & \text{if } (l,m) \in \mathcal{K} \quad l = 1, \ldots, L \\ 0 & \text{otherwise} \qquad\quad m = 1, \ldots, M. \end{cases} \tag{35}$$

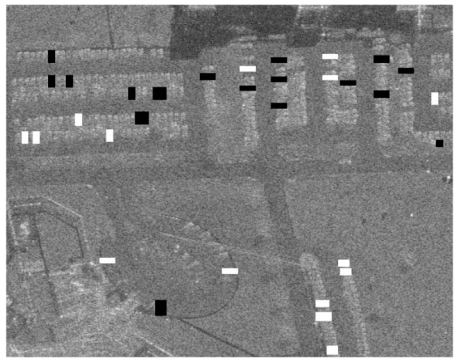

Fig. 8. Empirical ground truth superimposed to the reference image.

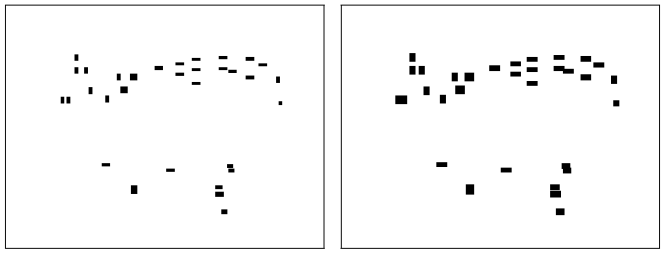

(a) (b)

Fig. 9. Empirical ground truth without/with the addition of guard cells. (a) Empirical ground truth. (b) Empirical ground truth with guard cells.

In Fig. 9(a), the empirical ground truth mask $\boldsymbol{G}(l,m)$ is shown. Although the acquisitions were performed during the same day and the images were registered, the returns from a scatterer contribute differently to neighbor pixels, e.g., a slightly different aspect angle can produce a different amount of energy spillover. These relative differences in the imaged data can lead to false alarms in the change detection results. In order to prevent a false alarm caused by pixel contamination by target returns, we consider a guard area around each arrival–departure. This allows the definition of an extended empirical ground truth [see Fig. 9(b)] used in the following to compare the performance of the considered detection algorithms.

In the following, a CFAR analysis based on the previously described real data is conducted. To this end, the thresholds are set to ensure $P_{\text{fa}} = 10^{-4}$ in the complement of the extended empirical ground truth area, namely, in the region where no changes occur (there are no true positives). This means that, for

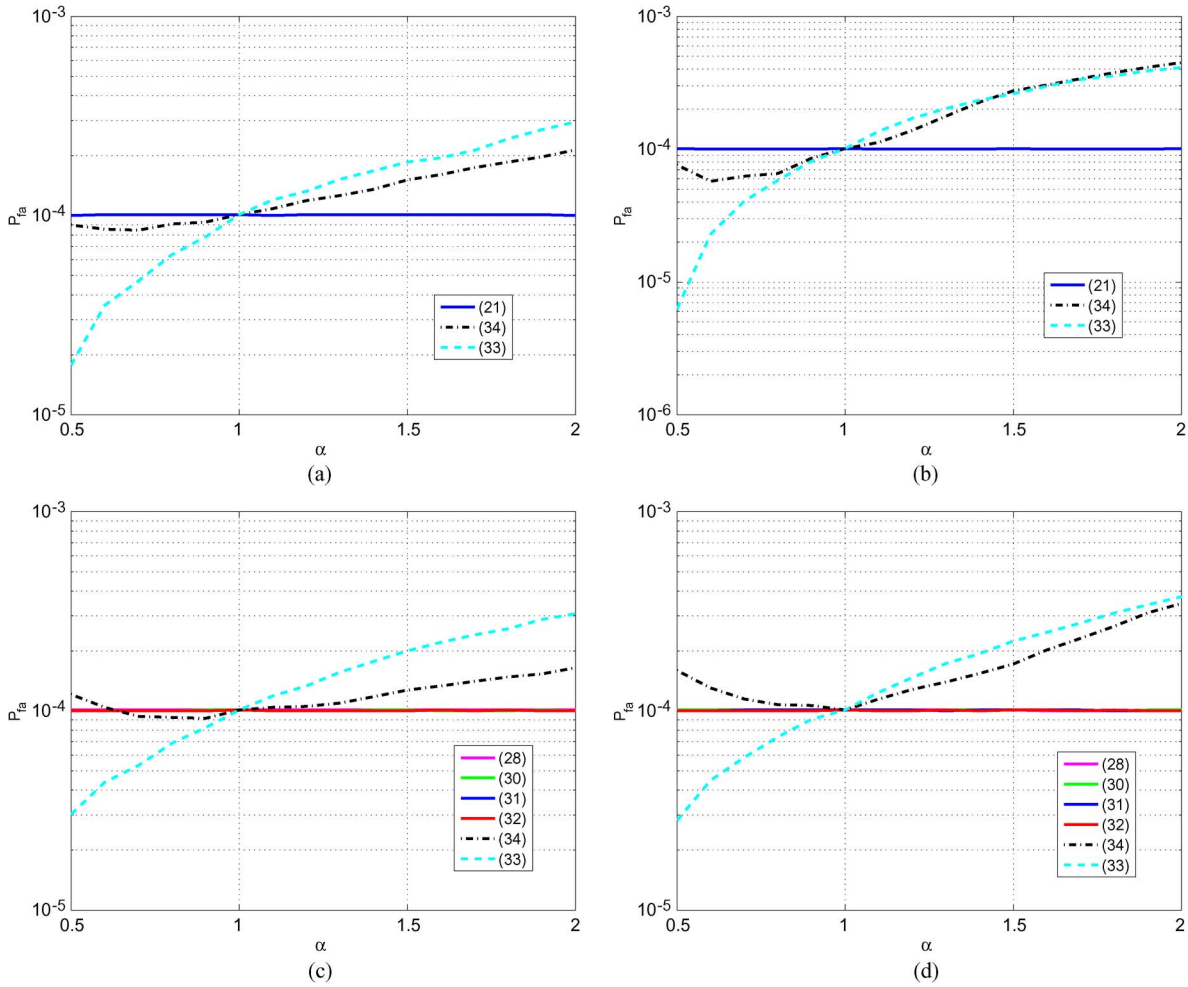

Fig. 10. P_{fa} versus α. (a) $N = 2, W = 3$. (b) $N = 2, W = 5$. (c) $N = 3, W = 3$. (d) $N = 3, W = 5$.

each detector, after computing the decision statistics (for each pixel belonging to the complement of the extended empirical ground truth), the threshold has been selected in order that

$$10^{-4} \times \text{total number of available statistics (trials)}$$

are greater than the threshold. This ensures that all of the comparisons refer to the same nominal P_{fa} level, namely, the number of threshold crossings in the complement of the extended empirical ground truth is exactly the same for all of the analyzed detectors. Then, exploiting the previously computed thresholds, the actual P_{fa} is estimated by applying a scaling $\sqrt{\alpha}$ to the test image for $\alpha \in [0.5, 2]$.

In Fig. 10, the P_{fa} versus α for $N = 2$ and $N = 3$ with inspection window sizes of $W = 3$ and $W = 5$ is shown.

The behaviors of the detectors (33) and (34) are also displayed. Confirming the simulated analysis, in all of the situations, the invariant detectors show to provide a stable probability of false alarm. The detectors (33) and (34) show poor ability to keep a CFAR in the presence of scale variations between the reference and test images. Specifically, they exhibit an actual P_{fa} different from the nominal value when a scale variation is present ($\alpha \neq 1$).

For the same scenarios, the number of correct detections in the extended empirical ground truth has been evaluated. The results are shown in Fig. 11; as expected, the scale-invariant detectors provide constant performance for different values of α, but in this case, they are outperformed by the detectors (33) and (34).

The final analysis investigates the effects of an aggregation strategy after single pixel detection in order to eliminate isolated false alarms and confirm true detections, which are due to the typical car size and system resolution, which appear quite often. More precisely, a window of size 5×5 slides along the horizontal and vertical dimensions of the detection maps (which, as already highlighted, are binary images: "0" no detection and "1" detection). Then, for a given pixel localized at the center of the moving window and labeled with "1," a detection is associated if the number of "1" in the window is greater that a certain integer "fill parameter" (denoted by F and complying with $1 \leq F \leq 25$).

These kinds of logics look like n-of-m aggregation techniques [25, Ch. 3] and can be interpreted as a postdetection binary integration within the reference window. As to the pixels on the image edge (namely, those lying on the first/last two rows or columns), no aggregation is performed because they never fall at the center of the moving window. In other words, the "0" or "1" value in the original detection map is simply confirmed.

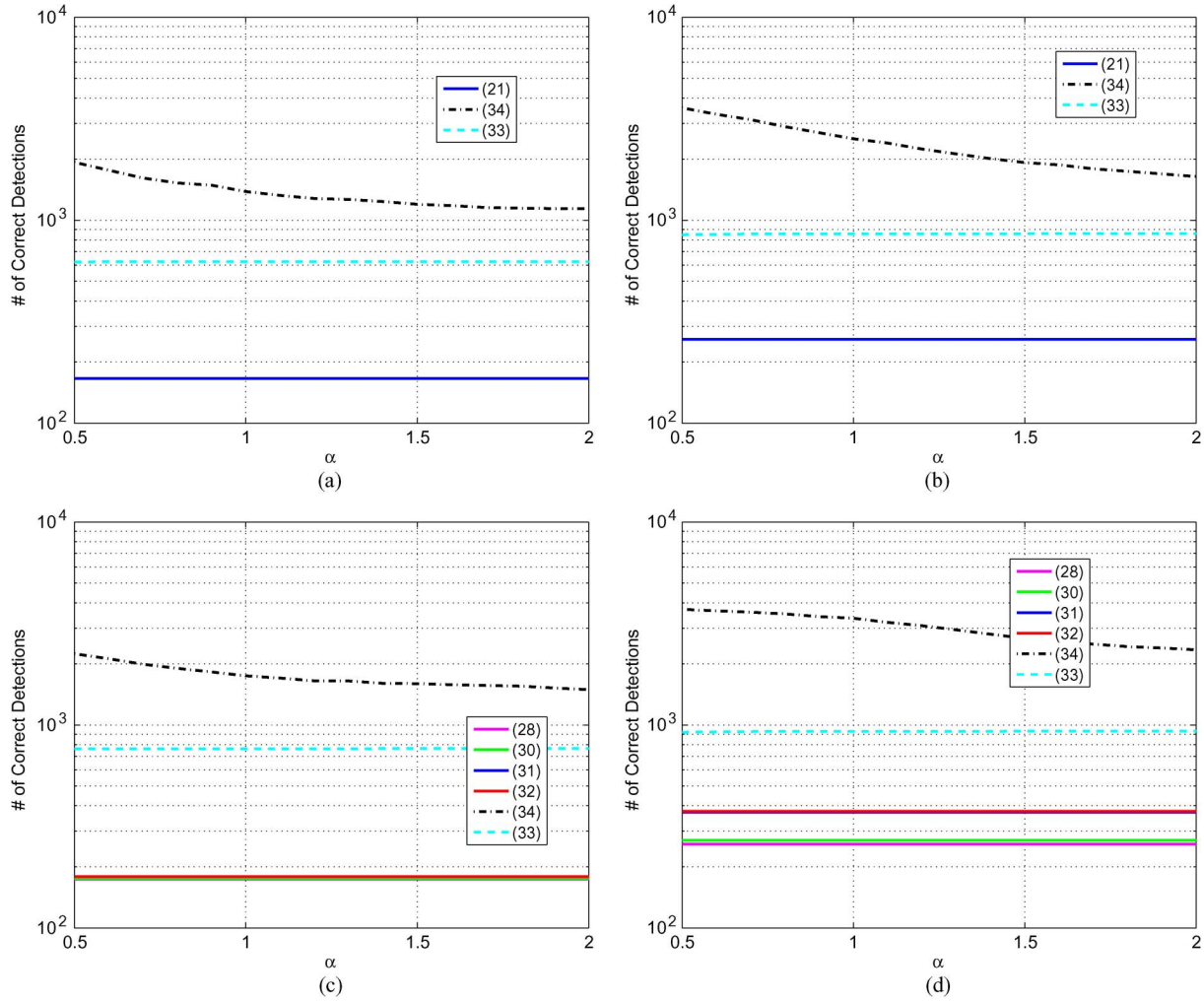

Fig. 11. Number of correct detections versus α. (a) $N = 2, W = 3$. (b) $N = 2, W = 5$. (c) $N = 3, W = 3$. (d) $N = 3, W = 5$.

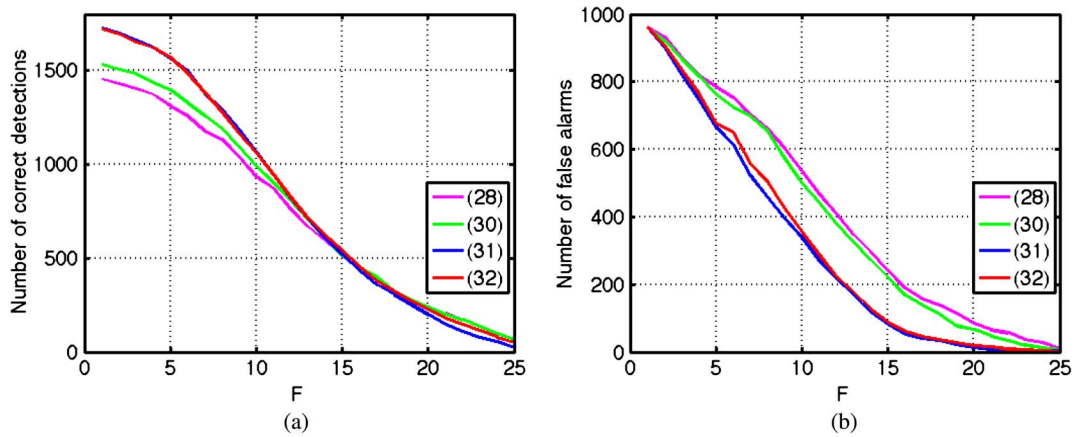

Fig. 12. (a) Number of correct detections in the extended empirical ground truth and (b) number of false alarms in the complement of the extended empirical ground truth versus F.

The case of three-polarimetric channels, with $W = 5$ and $\alpha = 1$, is considered, and the effect of the fill parameter is studied in Fig. 12 for detectors (28), (30)–(32). This analysis highlights that all of the proposed receivers are sensitive to the fill parameter value. Otherwise stated to get a lower number of false alarms through the aggregation procedure, it is necessary to accept some detection loss.

VI. Conclusion

In this paper, multipolarization scale-invariant change detection from SAR images has been considered. The problem has been formulated as a binary hypothesis test, and the principle of invariance has been applied to synthesize decision rules. This framework allows us to both enhance the robustness of the detectors with respect to intensity miscalibration effects and to

force the CFAR feature at the design stage. A maximal invariant statistic, which fully characterizes the class of invariant tests, as well as the induced maximal invariant was determined with reference to the processing of two- or three-polarimetric channels. Moreover, the GLRT is computed; interestingly for two-polarimetric channels, the test is equivalent to comparing the condition number of a data-dependent matrix with a suitable detection threshold. Further decision rules have been also introduced as combinations of the maximal invariant components.

At the analysis stage, the proposed framework has been assessed both on simulated data and on real high-resolution SAR images. The conducted study has shown the capability of the novel decision rules to provide the CFAR property even in the presence of power mismatches among the different acquisitions. The tradeoff between robustness and detection performance has also been discussed. Future work will perform an analysis of the new detectors as well as possible polarimetric extensions of other decision rules such as that in [27], in the presence of further real datasets collected under different environmental and operating conditions.

APPENDIX A

In this appendix, we show that the set of transformations G is a group. To this end, we define the *group multiplication* [20, p. 569] which with any two elements of G

$$g_1 = [\boldsymbol{B}_1, a_1 : \boldsymbol{B}_1 \in \mathcal{GL}(N), a_1 > 0] \in G$$
$$g_2 = [\boldsymbol{B}_2, a_2 : \boldsymbol{B}_2 \in \mathcal{GL}(N), a_2 > 0] \in G$$

associates the element

$$g_3 = [\boldsymbol{B}_1\boldsymbol{B}_2, a_1a_2 : \boldsymbol{B}_1\boldsymbol{B}_2 \in \mathcal{GL}(N), a_1a_2 > 0] \in G$$

called product and denoted as g_1g_2. It is easy to show the following.

1) *Group multiplication* obeys the associative law, i.e.,
$$(g_ag_b)g_c = g_a(g_bg_c), \qquad \forall\, g_a, g_b, g_c \in G.$$
2) The element
$$e_1 = [\mathbf{I}_N, 1] \in G$$
is the unique identity, namely, $ge_1 = e_1g = g\ \forall\, g \in G$.
3) $\forall\, g \in G$, there exists the unique inverse
$$g^{-1} = \left[\boldsymbol{B}^{-1}, a^{-1} : \boldsymbol{B}^{-1} \in \mathcal{GL}(N), a^{-1} > 0\right] \in G$$
such that $gg^{-1} = e_1$.

Hence, G satisfies the conditions which define a group [20, p. 569].

APPENDIX B

This appendix is devoted to the derivation of the $P_{\rm fa}$ and P_d for the GLRT exploiting $N = 2$ polarimetric channels. Under either H_0 and H_1, the test statistic in (21) is the standard condition number of a matrix following the so-called F distribution [19]. We begin providing its cumulative distribution function (CDF) under both hypotheses in the following

Proposition 2: Under H_0, the CDF of the test statistic (21) can be written as

$$F_\eta^0(x) = \frac{\beta}{\gamma^{2K}}\left[\int_0^{+\infty}\frac{\lambda^{K-2}}{(1+\lambda/\gamma)^{2K}}\int_\lambda^{x\lambda}\frac{u^K}{(1+u/\gamma)^{2K}}du\,d\lambda - 2\frac{\lambda^{K-1}}{(1+\lambda/\gamma)^{2K}}\int_\lambda^{x\lambda}\frac{u^{K-1}}{(1+u/\gamma)^{2K}}du\,d\lambda + \frac{\lambda^K}{(1+\lambda/\gamma)^{2K}}\int_\lambda^{x\lambda}\frac{u^{K-2}}{(1+u/\gamma)^{2K}}du\,d\lambda\right] \tag{36}$$

with $\beta = ((2K-1)/[(K-2)!]^2)\prod_{r=K}^{2K-2} r^2$. Under H_1

$$F_\eta^1(x) = \upsilon\beta\int_0^{+\infty}\sum_{\ell=1,k\neq\ell}^{2}\frac{(-1)^{\ell+1}\lambda^{K-2}}{(1+\lambda/\delta_\ell)^{2K-1}} \times\left[\int_\lambda^{x\lambda}\frac{u^{K-2}(u-\lambda)}{(1+u/\delta_k)^{2K-1}}du\right]d\lambda \tag{37}$$

where $\upsilon = (2K-1)/(\delta_1^{K-1}\delta_2^{K-1}(\delta_2-\delta_1))$, β is the same as in (36), and δ_i, $i = 1, 2$, is the ith eigenvalue of $\boldsymbol{\Sigma}_X\boldsymbol{\Sigma}_Y^{-1}$.

Proof: The CDF of the condition number of a matrix-variate whose joint eigenvalue distribution can be written as [26, Formula (6)]

$$f(\lambda) = K\det\left(\boldsymbol{\Phi}(\lambda)\right)\det\left(\boldsymbol{\Psi}(\lambda)\right)\prod_{\ell=1}^{2}\xi(\lambda_\ell) \tag{38}$$

can be obtained by exploiting [26, Formula (9)]. By inspection of the corresponding joint distribution of λ_1 and λ_2 under H_0, i.e., ([19, Formula (98)] with $\boldsymbol{\Omega} = \gamma\boldsymbol{I}$)

$$p(\lambda_1, \lambda_2) = \frac{\beta}{\gamma^{2K}}\prod_{i=1}^{2}\frac{\lambda_i^{K-2}}{(1+\lambda_j/\gamma)^{2K}}(\lambda_2-\lambda_1)^2 \tag{39}$$

and, respectively, under H_1 (see again [19, Formula (98)])

$$p(\lambda_1, \lambda_2) = \upsilon\beta\prod_{i=1}^{2}\lambda_i^{K-2}\det\left((1+\lambda_j/\delta_i)^{1-2K}\right)(\lambda_2-\lambda_1) \tag{40}$$

it is immediate to verify that both of the aforementioned laws are in the form (38). Henceforth, under H_0, the CDF takes the form

$$F_0(x) = \beta\int_0^{+\infty}\left\{\det\left(\mathbf{F}_1(\lambda)\right) + \det\left(\mathbf{F}_2(\lambda)\right)\right\}d\lambda \tag{41}$$

where the entries of the 2×2 matrices $\mathbf{F}_1$ and $\mathbf{F}_2$ are listed in the following, skipping for simplicity the subscript of λ

$$(\mathbf{F}_1)_{1,1} = \frac{\lambda^{K-2}}{(1+\lambda/\gamma)^{2K}} \quad (\mathbf{F}_1)_{1,2} = \frac{\lambda^{K-1}}{(1+\lambda/\gamma)^{2K}}$$

$$(\mathbf{F}_1)_{2,1} = \int_{\lambda}^{x\lambda} \frac{u^{K-1}}{(1+u/\gamma)^{2K}} du \quad (\mathbf{F}_1)_{2,2} = \int_{\lambda}^{x\lambda} \frac{u^{K}}{(1+u/\gamma)^{2K}} du$$

$$(\mathbf{F}_2)_{1,1} = \int_{\lambda}^{x\lambda} \frac{u^{K-2}}{(1+u/\gamma)^{2K}} du \quad (\mathbf{F}_2)_{1,2} = \int_{\lambda}^{x\lambda} \frac{u^{K-1}}{(1+u/\gamma)^{2K}} du$$

$$(\mathbf{F}_2)_{2,1} = \frac{\lambda^{K-1}}{(1+\lambda/\gamma)^{2K}} \quad (\mathbf{F}_2)_{2,2} = \frac{\lambda^{K-2}}{(1+\lambda/\gamma)^{2K}}.$$

Under H_1, instead, the CDF can be expressed as

$$F_1(x) = \upsilon\beta \int_0^{+\infty} \left\{ \det\left(\mathbf{G}_1(\lambda)\right) + \det\left(\mathbf{G}_2(\lambda)\right) \right\} d\lambda \qquad (42)$$

where the entries of the 2×2 matrix $\mathbf{G}_i$, $i = 1, 2$, are given by

$$(\mathbf{G}_1)_{1,1} = \frac{\lambda^{K-2}}{(1+\lambda/\delta_1)^{2K-1}}$$

$$(\mathbf{G}_1)_{1,2} = \frac{\lambda^{K-1}}{(1+\lambda/\delta_1)^{2K-1}}$$

$$(\mathbf{G}_1)_{2,1} = \int_{\lambda}^{x\lambda} \frac{u^{K-2}}{(1+u/\delta_2)^{2K-1}} du$$

$$(\mathbf{G}_1)_{2,2} = \int_{\lambda}^{x\lambda} \frac{u^{K-1}}{(1+u/\delta_2)^{2K-1}} du$$

$$(\mathbf{G}_2)_{1,1} = \int_{\lambda}^{x\lambda} \frac{u^{K-2}}{(1+u/\delta_1)^{2K-1}} du$$

$$(\mathbf{G}_2)_{1,2} = \int_{\lambda}^{x\lambda} \frac{u^{K-1}}{(1+u/\delta_1)^{2K-1}} du$$

$$(\mathbf{G}_2)_{2,1} = \frac{\lambda^{K-2}}{(1+\lambda/\delta_2)^{2K-1}}$$

$$(\mathbf{G}_2)_{2,2} = \frac{\lambda^{K-1}}{(1+\lambda/\delta_2)^{2K-1}}.$$

Hence, basic algebra leads to Proposition 2 statement.

As an immediate consequence of Proposition 2, we can now prove the following.

Proposition 3: P_{fa} and P_d of the GLRT (21) are given by

$$P_{\mathrm{fa}} = 1 - \beta \left[\mathcal{J}(0) - 2\mathcal{J}(1) + \mathcal{J}(2) \right] \qquad (43)$$

where β is the same as in Proposition 2, T_2 is the detection threshold, and for $\ell = 0, 1, 2$

$$\mathcal{J}(\ell) = \int_0^{+\infty} \frac{z^{K+\ell-2}}{(1+z)^{2K}} \int_z^{T_2} \frac{y^{K-\ell}}{(1+y)^{2K}} dy\, dz \qquad (44)$$

and by

$$P_d = 1 - (2K-1)\upsilon\beta \int_0^{+\infty} z^{K-2} \left[\int_z^{T_2} \frac{y^{K-2}(y-z)}{(1+y)^{2K-1}} dy \right] \times \left[\frac{\delta_2^{2K-1}}{(1+z/\omega)^{2K-1}} - \frac{\delta_1^{2K-1}}{(1+z\omega)^{2K-1}} \right] dz \qquad (45)$$

with $\omega = \delta_1/\delta_2$.

Proof: Proposition 3 follows immediately from Proposition 2, expanding the determinant in the argument of (39) and (40) for P_{fa} and for P_d, respectively. As expected, P_{fa} does not depend on the scaling factor γ, and P_d only depends on $\omega = \delta_1/\delta_2$, after replacing υ by its expression as a function of δ_i's, $i = 1, 2$.

REFERENCES

[1] M. Preiss and N. J. S. Stacy, "Coherent Change Detection: Theoretical Description and Experimental Results," Intell., Surveillance Reconnaissance Division, Def. Sci. Technol. Org., Canberra, Australia, DSTO-TR-1851, 2006.

[2] R. Touzi, A. Lopes, J. Bruniquel, and P. W. Vachon, "Coherence estimation for SAR imagery," *IEEE Trans. Geosci. Remote Sens.*, vol. 37, no. 1, pp. 135–149, Jan. 1999.

[3] I. Stojanovic and L. Novak, "Change detection experiments using Gotcha public release SAR data," in *Proc. SPIE, Algorithms for Synthetic Aperture Radar Imagery XX*, Jun. 3, 2013, vol. 8746, p. 87460I, DOI: 10.1117/12.2020650

[4] E. J. M. Rignot and J. J. Van Zyl, "Change detection techniques for ERS-1 SAR data," *IEEE Trans. Geosci. Remote Sens.*, vol. 31, no. 4, pp. 896–906, Jul. 1993.

[5] K. Conradsen, A. A. Nielsen, J. Schou, and H. Skriver, "A test statistic in the complex Wishart distribution and its application to change detection in polarimetric SAR data," *IEEE Trans. Geosci. Remote Sens.*, vol. 41, no. 1, pp. 4–19, Jan. 2003.

[6] L. M. Novak, "Change detection for multipolarization, multipass SAR," in *Proc. SPIE Conf. Algorithms Synthetic Aperture Radar Imagery XII*, Orlando, FL, USA, Mar. 2005, pp. 234–246.

[7] A. Reigber *et al.*, "Very-high-resolution airborne synthetic aperture radar imaging: Signal processing and applications," *Proc. IEEE*, vol. 101, no. 3, pp. 759–783, Mar. 2013.

[8] A. Marino, S. R. Cloude, and J. M. Lopez-Sanchez, "A new polarimetric change detector in radar imagery," *IEEE Trans. Geosci. Remote Sens.*, vol. 51, no. 5, pp. 2986–3000, May 2013.

[9] A. A. Nielsen, R. Larsen, and H. Skriver, "Change detection in bitemporal EMISAR data from Kalø, Denmark, by means of canonical correlations analysis," in *Proc. 3rd Int. Airborne Remote Sens. Conf. Exhib.*, Copenhagen, Denmark, Jul. 7–10, 1997, pp. 281–287.

[10] A. A. Nielsen, "Change detection in multispectral bi-temporal spatial data using orthogonal transformations," in *Proc. 8th Austral-Asian Sens. Conf.*, Canberra, ACT, Australia, Mar. 25–29, 1996, pp. 1–8.

[11] E. Erten, A. Reigber, L. Ferro-Famil, and O. Hellwich, "A new coherent similarity measure for temporal multichannel scene characterization," *IEEE Trans. Geosci. Remote Sens.*, vol. 50, no. 7, pp. 2839–2851, Jul. 2012.

[12] V. Carotenuto, A. De Maio, C. Clemente, and J. J. Soraghan, "Multipolarization SAR change detection with invariant decision rules," in *Proc. IEEE Radarcon*, Cincinnati, OH, USA, May 19–23, 2014, pp. 0859–0862.

[13] V V. Carotenuto, A. De Maio, C. Clemente, and J. J. Soraghan, "Invariant rules for multi-polarization SAR change detection," *IEEE Trans. Geosci. Remote Sens.*, vol. 53, no. 6, pp. 3294–3311, Jun. 2015.

[14] "Coherent Change Detection Challenge Problem," U.S. Air Force Sensor Data Management System, Arlington, VA, USA. [Online]. Available: https://www.sdms.afrl.af.mil/index.php?collection=ccd_challenge

[15] S. Scarborough *et al.*, "A challenge problem for SAR change detection and data compression," in *Proc. SPIE, Algorithms for Synthetic Aperture Radar Imagery XVII*, Apr. 18, 2010, vol. 7699, p. 76990U.

[16] S. N. Anfinsen, A. P. Doulgeris, and T. Eltoft, "Estimation of the equivalent number of looks in polarimetric synthetic aperture radar imagery,"

IEEE Trans. Geosci. Remote Sens., vol. 47, no. 11, pp. 3795–3809, Nov. 2009.
[17] C. Lopez-Martinez, "Speckle noise characterization and filtering in polarimetric SAR data," Eur. Space Agency, Paris, France. [Online]. Available: https://earth.esa.int/documents/10174/669756/Speckle_Noise_Characterisation.pdf
[18] S. M. Kay, *Fundamentals of Statistical Signal Processing: Estimation Theory*, vol. 1. Upper Saddle River, NJ, USA: Prentice-Hall, 1998.
[19] A. T. James, "Distribution of matrix variates and latent roots derived from normal samples," *Annals of Mathematical Statistics*, vol. 35, no. 2, pp. 475–501, Jun. 1964.
[20] E. L. Lehmann, *Testing Statistical Hypotheses*. 2nd ed., New York, NY, USA: Springer-Verlag, 1986.
[21] R. J. Muirhead, *Aspects of Multivariate Statistical Theory*. New York, NY, USA: Wiley, 1982.
[22] L. L. Scharf, *Statistical Signal Processing. Detection, Estimation, and Time Series Analysis*. Reading, MA, USA: Addison-Wesley, 1991.
[23] A. Marino and I. Hajnsek, "A change detector based on an optimization with polarimetric SAR imagery," *IEEE Trans. Geosci. Remote Sens.*, vol. 52, no. 8, pp. 4781–4798, Aug. 2014.
[24] R. A. Horn and C. R. Johnson, *Matrix Analysis*. Cambridge, MA, USA: Cambridge Univ. Press, 1985.
[25] M. A. Richards, J. A. Scheer, and W. A. Holm, *Principles of Modern Radar: Basic Principles*. Raleigh, NC, USA: Scitech Publishing, 2010.
[26] M. Matthaiou, M. R. Mc Kay, P. J. Smith, and J. A. Nossek, "On the condition number distribution of complex Wishart matrices," *IEEE Trans. Commun.*, vol. 58, no. 6, pp. 1705–1717, Jun. 2010.
[27] J. Inglada and G. Mercier, "A new statistical similarity measure for change detection in multitemporal SAR images and its extension to multiscale change analysis," *IEEE Trans. Geosci. Remote Sens.*, vol. 45, no. 5, pp. 1432–1445, May 2007.

Vincenzo Carotenuto (S'12) received the Laurea Specialistica degree in telecommunication engineering from the University of Naples "Federico II," Napoli, Italy, in 2010 and the Ph.D. degree in electronic and telecommunication engineering from the Department of Electrical Engineering and Information Technologies, University of Naples "Federico II," in 2015.

His research interest lies in the field of statistical signal processing, with emphasis on radar signal processing.

Antonio De Maio (S'01–A'02–M'03–SM'07–F'13) was born in Sorrento, Italy, on June 20, 1974. He received the Dr.Eng. degree (with honors) and the Ph.D. degree in information engineering from the University of Naples "Federico II," Napoli, Italy, in 1998 and 2002, respectively.

From October to December 2004, he was a Visiting Researcher with the U.S. Air Force Research Laboratory, Rome, NY, USA. From November to December 2007, he was a Visiting Researcher with the Chinese University of Hong Kong, Hong Kong. He is currently an Associate Professor with the University of Naples "Federico II." His research interest lies in the field of statistical signal processing, with emphasis on radar detection, optimization theory applied to radar signal processing, and multiple-access communications.

Dr. De Maio was the recipient of the 2010 IEEE Fred Nathanson Memorial Award as the young (less than 40 years of age) AESS Radar Engineer 2010 whose performance is particularly noteworthy as evidenced by contributions to the radar art over a period of several years, with the following citation for "robust CFAR detection, knowledge-based radar signal processing, and waveform design and diversity."

Carmine Clemente (S'09–M'13) received the Laurea (B.Sc.; *cum laude*) and Laurea Specialistica (M.Sc.; *cum laude*) degrees in telecommunications engineering from Universita' degli Studi del Sannio, Benevento, Italy, in 2006 and 2009, respectively, and the Ph.D. degree from the University of Strathclyde, Glasgow, U.K., in 2012.

He is currently a Research Associate with the Department of Electronic and Electrical Engineering, University of Strathclyde, working on advanced radar signal processing algorithms, MIMO radar systems, and micro-Doppler analysis. His research interests include synthetic aperture radar (SAR) focusing and bistatic SAR focusing algorithm development, micro-Doppler signature analysis and extraction from multistatic radar platforms, micro-Doppler classification, and statistical signal processing.

John J. Soraghan (S'83–M'84–SM'96) received the B.Eng. (Hons.) and M.Eng.Sc. degrees in electronic engineering from University College Dublin, Dublin, Ireland, in 1978 and 1983, respectively, and the Ph.D. degree in electronic engineering from the University of Southampton, Southampton, U.K., in 1989. His doctoral research focused on synthetic aperture radar processing on the distributed array processor.

After graduating, he worked with the Electricity Supply Board in Ireland and with Westinghouse Electric Corporation in the U.S. In 1986, he joined the Department of Electronic and Electrical Engineering, University of Strathclyde, Glasgow, U.K., as a Lecturer, where he became a Senior Lecturer in 1990, a Reader in 2000, and a Professor of signal processing in September 2003, within the Institute for Communications and Signal Processing (ICSP). In December 2005, he became the Head of the ICSP. He currently holds the Texas Instruments Chair in Signal Processing with the University of Strathclyde. He was a Manager of the Scottish Transputer Centre from 1988 to 1991 and a Manager of the DTI Parallel Signal Processing Centre from 1991 to 1995. His main research interests are signal processing theories, algorithms, and architectures with applications to remote sensing, telecommunications, biomedicine, and condition monitoring.

Prof. Soraghan is a member of the IET.

Giusi Alfano received the Laurea degree in communication engineering from the University of Naples "Federico II," Napoli, Italy, in 2001 and the Ph.D. degree in information engineering from the University of Benevento, Benevento, Italy, in 2007.

She is currently holding a postdoctoral position at Politecnico di Torino, Torino, Italy. Her research work lies mainly in the field of random matrix theory applications to MIMO wireless communications and sensor networks, and to the characterization of the physical layer of random networks. She was a Visiting Researcher at FTW and TUW, Wien, Austria, from 2007 to 2010 and an ERCIM fellow at NTNU Trondheim in 2011. In 2014, she was the Visiting ERC Chair on Noncommutative Distributions in Quantum Probability, Saarbrucken, Germany. She actively collaborates with the Theoretic Communication Chair, Dresden, Germany.